INTERFACE

royalsocietypublishing.org/journal/rsif

Research

Cite this article: Millane RP, Wojtas DH, Hong Yoon C, Blakeley ND, Bones PJ, Goyal A, Squire JM, Luther PK. 2021 Geometric frustration in the myosin superlattice of vertebrate muscle. *J. R. Soc. Interface* **18**: 20210585.
https://doi.org/10.1098/rsif.2021.0585

Received: 15 July 2021
Accepted: 16 November 2021

Subject Category:
Life Sciences–Physics interface

Subject Areas:
biophysics

Keywords:
vertebrate muscle, geometric frustration, myosin, antiferromagnet, Ising model

Author for correspondence:
Rick P. Millane
e-mail: rick.millane@canterbury.ac.nz

†C.H.Y. current address: SLAC National Accelerator Laboratory, Menlo Park, CA 94025, USA.

‡This paper is dedicated to our friend, colleague and coauthor Professor John Squire, who sadly died from COVID-19 on 31 January 2021. John was a giant in muscle research, and literally 'wrote the textbook' in the field. Equally, he was a true gentleman: generous of spirit, delightful and engaging company, and dedicated to science, and to his friends, colleagues and family alike. He is greatly missed.

Electronic supplementary material is available online at https://doi.org/10.6084/m9.figshare.c.5731065.

THE ROYAL SOCIETY PUBLISHING

Geometric frustration in the myosin superlattice of vertebrate muscle

Rick P. Millane[1], David H. Wojtas[1], Chun Hong Yoon[1,†], Nicholas D. Blakeley[1], Philip J. Bones[1], Abhishek Goyal[1], John M. Squire[2,‡] and Pradeep K. Luther[3]

[1]Computational Imaging Group, Department of Electrical and Computer Engineering, University of Canterbury, Private Bag 4800, Christchurch, New Zealand
[2]Muscle Contraction Group, School of Physiology, Pharmacology and Neuroscience, University of Bristol, Bristol BS8 1TD, UK
[3]National Heart and Lung Institute, Sir Alexander Fleming Building, Imperial College London, London SW7 2AZ, UK

RPM, 0000-0003-2226-5774

Geometric frustration results from an incompatibility between minimum energy arrangements and the geometry of a system, and gives rise to interesting and novel phenomena. Here, we report geometric frustration in a native biological macromolecular system—vertebrate muscle. We analyse the disorder in the myosin filament rotations in the myofibrils of vertebrate striated (skeletal and cardiac) muscle, as seen in thin-section electron micrographs, and show that the distribution of rotations corresponds to an archetypical geometrically frustrated system—the triangular Ising antiferromagnet. Spatial correlations are evident out to at least six lattice spacings. The results demonstrate that geometric frustration can drive the development of structure in complex biological systems, and may have implications for the nature of the actin–myosin interactions involved in muscle contraction. Identification of the distribution of myosin filament rotations with an Ising model allows the extensive results on the latter to be applied to this system. It shows how local interactions (between adjacent myosin filaments) can determine long-range order and, conversely, how observations of long-range order (such as patterns seen in electron micrographs) can be used to estimate the energetics of these local interactions. Furthermore, since diffraction by a disordered system is a function of the second-order statistics, the derived correlations allow more accurate diffraction calculations, which can aid in interpretation of X-ray diffraction data from muscle specimens for structural analysis.

1. Introduction

Geometric frustration results from an incompatibility of neighbour minimum energy arrangements with the topology of the bulk system [1–6]. It leads to highly degenerate ground states and novel phases of matter, and is recognized as an important organizing principle in systems including spin glasses, superconductors, protein crystals, quantum dynamics, colloids, plasmonics, protein folding and neural computation [7–15]. The presence of geometric frustration in experimental systems is frequently inferred indirectly by methods such as X-ray scattering, NMR, heat capacity and susceptibility [16]. It has also been observed directly using fabricated arrays of superconducting rings [7], nanoscale magnets [8,17–21] and confined colloidal monolayers [22]. Geometric frustration has most frequently been observed in either natural or fabricated physical systems. In this paper, we report the presence of geometric frustration in a native biological macromolecular system—the myosin lattice of vertebrate muscle. We show that the observed disorder in the myosin filament array is well-modelled by an archetypical frustrated system, the triangular Ising antiferromagnet (TIA). Mapping this system to an Ising model allows the extensive results on this model to be used to explore relationships between local interactions and long-range order, the energetics of intermolecular interactions and possible

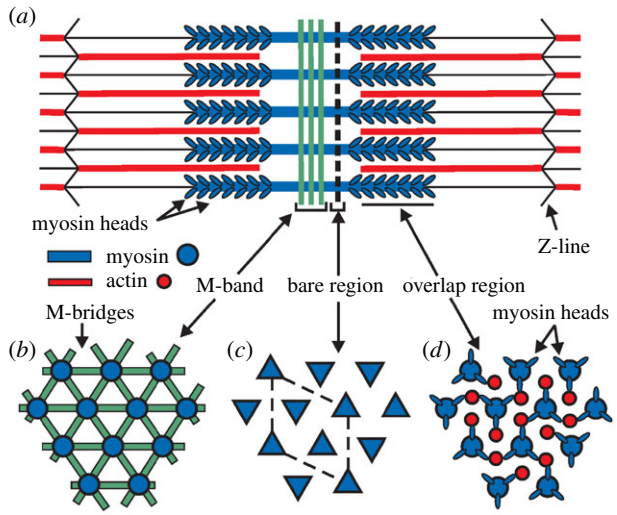

Figure 1. Schematic diagram of a muscle sarcomere (the repeating unit of a myofibril). (*a*) The overlapping myosin and actin filaments, the cross-linking of the myosin filaments at the M-band and the location of the bare region (dashed line) between the M-band and where the myosin head array starts on the myosin filaments. (*b–d*) Cross-sections through various parts of the sarcomere in (*a*), showing (*b*) the M-band where M-bridges cross-link the myosin filaments, (*c*) the bare region where the myosin filaments appear triangular (a superlattice cell is shown by the dashed lines) and (*d*) the crossbridge, or overlap, region where the myosin heads project from the myosin filament backbone. (Figure redrawn from [28,33].)

implications for biological function, and derivation of other physical quantities such as diffraction properties.

The molecular basis of muscle contraction is an ongoing area of research [23–27]. At the molecular level, the key components that mediate contraction are the proteins myosin and actin. The myosin and actin molecules assemble together to form myosin and actin filaments, which are often referred to as the thick filaments and thin filaments, respectively. Muscle myosin consists of a two-chain α-helical rod with a globular 'head' at one end of each chain. The two globular heads are in close proximity at one end of the resulting dimer, and when assembled in the myosin filament, the myosin heads decorate the filament surface. The myosin and actin filaments pack together side-by-side in an interdigitated array, and the arrays are assembled end-to-end to form long assemblies called myofibrils [28,29]. The end-to-end assembly results in a periodic structure, and the repeating unit is referred to as the sarcomere. The sarcomere is the basic contractile unit of vertebrate striated (skeletal and cardiac) muscle. In vertebrate muscle, myofibril cross-sections vary in size and shape, measure 2–5 µm across, and in humans can be up to approximately 0.1 m long. Several hundred myofibrils are bundled together to form a muscle fibre, and vertebrate muscle is composed of approximately parallel bundles of thousands of muscle fibres.

Muscular force is generated by a series of biochemical reactions that result in a force and sliding movement between the actin and myosin filaments [28,30]. This results from cycles in which myosin heads that project from the myosin filament surface attach to actin, undergo a structural transition that produces the relative force and movement, and are subsequently released from actin [28–32]. This attachment/detachment cycle is repeated, providing muscular force generation and contraction.

The geometrical relationship between the myosin and actin filaments in the sarcomere is shown in figure 1. The interactions between the myosin heads and the actin filaments occur in the so-called overlap or crossbridge region where the two filaments are side-by-side, as shown in figure 1. Three other relevant regions of the sarcomere are the bare region, where there are myosin filaments but no myosin crossbridges, the M-band region, where the myosin filaments are cross-linked and anchored together, and the Z-line boundary between two contiguous sarcomeres, also shown in figure 1.

In cross-section, the myosin filaments are arranged on a triangular lattice (figure 1). The arrangement of the myosin filaments on this lattice is not perfectly regular however, each filament adopting one of two rotations about its long axis, with the two rotations being distributed on the lattice in a disordered, semi-random manner. This disorder is referred to as the myosin superlattice [33]. It is the nature of this myosin superlattice disorder with which we are concerned.

The superlattice disorder in muscle is described in §2. In §3, we describe our measurement of the filament rotation disorder and its analysis in terms of the TIA. A tentative interpretation in terms of the energetics of myosin filament interactions and concluding remarks are given in §4.

2. The myosin superlattice

The myosin filaments in vertebrate muscle are arranged in the myofibrils on a triangular array with a spacing of approximately 47 nm [31,34], with the actin filaments interdigitated within the myosin array at the centre of each triangle (figure 1). The myosin filaments themselves exhibit internal threefold rotational symmetry and exhibit an approximately triangular cross-section in the bare region. This is most clearly seen in electron micrographs of thin transverse sections through the bare region, where there is less clutter from the other molecular components. An example micrograph through the bare region of one myofibril of frog sartorius muscle is shown in figure 2*a*. The closed disordered contour seen in the micrograph (and marked by the blue curve) is the boundary of the myofibril. Within the myofibril, the triangular lattice is clearly evident and the dark, approximately triangular, regions are the cross-sections of the myosin filaments. Close inspection of such micrographs shows that in the striated muscles of higher vertebrates, the myosin filaments adopt one of two rotations about their long axis, which are 60° (or 180°, as a result of their threefold symmetry) apart. The two rotations are distributed on the lattice in a semi-systematic manner [33]. This is the myosin superlattice disorder.

Although the superlattice disorder is frequently seen in vertebrate muscle, there are exceptions where all the myosin filaments have the same rotation, which is referred to as the simple lattice. The simple lattice is seen in bony fish muscles [35], slow muscles of sharks (cartilaginous fish) [36] and the rat soleus muscle [37]. Furthermore, in other cases, particularly in the activated state, the myosin lattice may be subject to lattice disorder or disorder in the population of the cross-bridges, possibly masking the presence of either a simple or superlattice [38–40].

The spatial arrangement of the myosin filament rotations in vertebrate muscle has been studied by Luther & Squire [33]. By manual inspection of the micrographs, they determined the rotation of each filament and analysed the neighbourhood relationships of the rotations. They found that the filament rotations tend to follow two rules, which

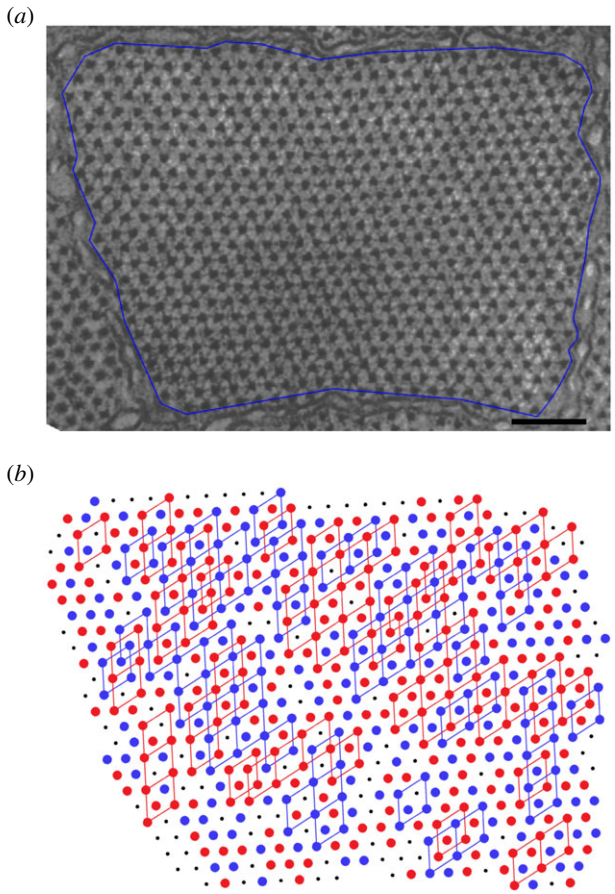

Figure 2. (*a*) Electron micrograph of a thin section through the bare region of one myofibril of frog sartorius muscle. The blue line shows the boundary of the myofibril within which the filament rotations were determined. The scale bar is 200 nm. (*b*) Myosin filament rotations derived from (*a*). The red and blue circles denote the two rotations and the small black dots denote filaments with unknown orientations. The superlattice structure is shown by the rhombi whose vertices are second nearest-neighbour filaments with the same rotation.

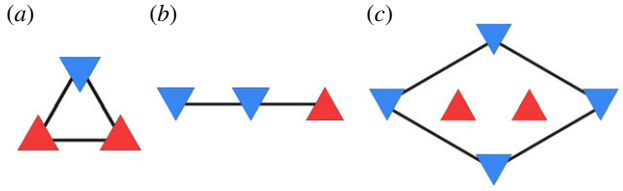

Figure 3. The no-three-alike rules, (*a*) Rule 1 and (*b*) Rule 2. (*c*) The rhombahedral unit cell of the superlattice, as described in the text.

they referred to as the no-three-alike rules. The first rule (Rule 1) is that the three mutually adjacent filaments at the corners of an elementary triangle in the lattice usually do not all have the same rotation (figure 3*a*). The second rule (Rule 2) is that the three adjacent filaments along a row in the lattice usually do not all have the same rotation (figure 3*b*). Using simple lattice constructions based on these two rules, they showed that they generate lattices in which the filament rotations at the corners of a rhombus of side length $\sim 81 \simeq 47\sqrt{3}$ nm, whose edges join second-nearest-neighbours in the lattice, tend to be the same (figure 3*c*). The rhombohedral unit cell, which contains three myosin filaments, generates a triangular lattice, referred to as the superlattice, of spacing approximately 81 nm.

We have previously reported an attempt to derive a more quantitative model of the myosin lattice disorder than the empirical no-three-alike rules, by analysing the filament rotational disorder in the same micrograph as that of Luther & Squire [33] in terms of a model based on the TIA [41,42]. Although suggestive, limited results were obtained for data from only a few micrographs from a single species. Comparison with the TIA used Monte Carlo simulation and a simplified model of the TIA correlation structure. Here, we present an extended and detailed analysis using a dataset comprising micrographs of 15 myofibrils from 4 vertebrate species, and using accurate analytical expressions for the TIA spatial correlation function. This has allowed a more detailed comparison with the sublattice structure of the TIA second-order statistics and more definitive conclusions. The results provide strong evidence that the TIA is a universal model for the superlattice disorder in vertebrate striated muscle.

There is good evidence that the superlattice structure seen in the bare region extends into the overlap and M-band regions of the sarcomere. Electron microscopy shows presence of the superlattice in different parts of the A-band, which include the M-band, the bare region and the filament tip region [35], and X-ray fibre diffraction patterns of whole muscle fibres show reflections with spacings based on the approximately 81 nm lattice [31]. The superlattice structure is therefore expected to be related to the nature of the myosin head–actin interactions in the overlap region. It has been proposed that the superlattice structure leads to a more efficient sharing of actin-binding sites by myosin heads than occurs in simple lattice muscles [33,36]. The spatial arrangement of the myosin filament rotations in relation to the neighbouring filaments may be related to stereospecific binding of myosin heads to actin and the influence of the actin target areas [43]. The superlattice disorder is therefore of intrinsic interest in terms of the development of the sarcomere and muscle function.

Analysis of X-ray diffraction patterns from muscle specimens has been an important technique for studying the molecular structures of muscle and muscle components [28,32,34,40,44]. Such analysis depends on accurate calculation of the diffraction from model structures for comparison with the observed diffraction. However, the observed diffraction from a disordered system is a function of the nature of the disorder, and in particular of the second-order statistics [45–47], so that calculation of diffraction from model structures must also incorporate the effects of the disorder. An approximate model of the superlattice disorder has been used to partially account for its effects on diffraction calculations [48], but this model does not capture all the subtleties of the TIA disorder. The full second-order statistics (correlations) provided by the TIA model will allow the development of methods to accurately account for the disorder in diffraction calculations. Some work in this direction for a 2D lattice has been reported [49], but this will need to be extended to a full 3D calculation with molecular models and cylindrical averaging for application to muscle diffraction. While a significant undertaking, the results presented here provide the basis for making such a calculation.

3. Analysis of the myosin lattice disorder

3.1. Myosin filament orientations

We characterize the nature of the myosin lattice disorder by measuring the filament rotations and analysing their

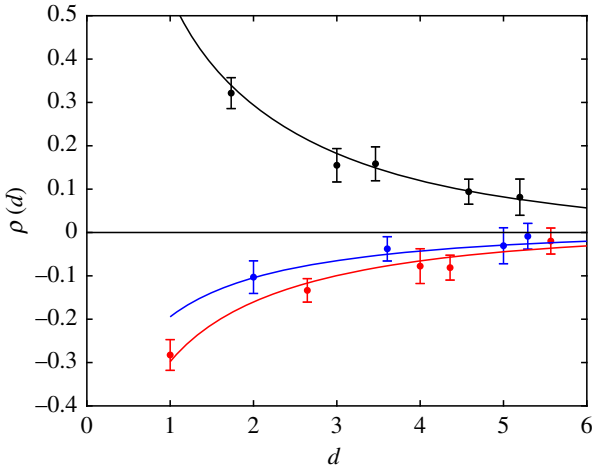

Figure 4. Correlation coefficient versus separation d calculated from the frog sartorious muscle 1 myofibril (filled circles) with error bars at the 95% confidence interval shown. The calculated TIA correlation function at $T = 0.53$ is shown by the full curves, with the three colours representing sites on the three sublattices: sublattice 0 (black), sublattice 1 (blue), sublattice 2 (red).

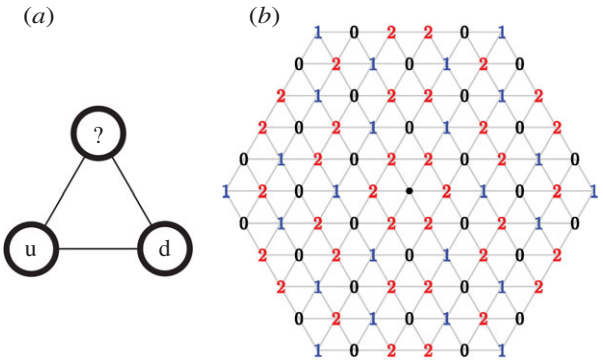

Figure 5. (*a*) Frustration on an elementary triangular domain. Up (u) and down (d) adjacent spins are preferred. It is not possible to optimize all interactions, leading to geometric frustration. (*b*) Sublattice structure of the TIA with the sites of the three sublattices labelled 0, 1 and 2 [51]. The origin, on sublattice 0, is marked by the filled circle. A precise definition of the sublattices is given in Appendix A.

second-order statistics. A dataset consisting of electron micrographs of 15 myofibrils was used for this purpose. Specimen preparation and electron microscopy were as described by Luther & Squire [33] and summarized in the electronic supplementary material. Data were obtained from 9 myofibrils from frog sartorius muscle, 3 from shark white myotomal muscle, one from turtle leg muscle and two from polypterus white myotomal muscle. These examples give a broad representation of the vertebrate family. The micrograph shown in figure 2*a* is one of the frog sartorius muscle examples, which we use to illustrate the analysis. The other micrographs (see electronic supplementary material) were treated in an analogous fashion.

Measurement and classification of the fibril rotations in the micrographs were achieved using an automated image analysis procedure designed for this purpose [50]. Using this method, the rotation of each filament in a myofibril cross-section is determined and classified into one of the two rotations, or classified as indeterminate if its rotation cannot be reliably determined. The result of this analysis for the micrograph shown in figure 2*a* is shown in figure 2*b*. Filament classifications for all micrographs are included in the electronic supplementary material. The myofibril in figure 2*a* contains 653 filaments. The rotations of 552 filaments were determined unambiguously, and those of the remaining 101 filaments were indeterminate. The derived filament rotations and superlattice cells are shown in figure 2*b*.

The second-order statistics of the filament rotations for each myofibril were determined by calculating the spatial correlation $\rho(\mathbf{d})$, where

$$\rho(\mathbf{d}) = \langle s_{\mathbf{a}}, s_{\mathbf{a}+\mathbf{d}} \rangle_{\mathbf{a}}, \tag{3.1}$$

$s_{\mathbf{a}} = \pm 1$ for the two different rotations at the site with vector position $\mathbf{a}$ (in units of the lattice spacing), $\mathbf{d}$ is the vector separation, of length d, between the two sites, and $\langle \cdot \rangle_{\mathbf{a}}$ denotes ensemble averaging over positions $\mathbf{a}$ in the myofibril.

The correlations, versus the distance d between the lattice sites, for the filament rotations in figure 2 are shown by the filled circles in figure 4. Error bars at the 95% confidence interval (2 s.e.) are also shown. The reason for plotting the correlations versus the distance d, rather than the vector separation $\mathbf{d}$, and the significance of the three colours in the plot, are described in the next subsection. Significant, i.e. non-zero, correlations are seen out to six lattice spacings. Close inspection of figure 4 shows a pattern in which the correlations alternate between positive and negative values, and decay, with increasing distance d. This non-zero and structured correlation function points to a specific, i.e. non-random, distribution of filament rotations. Similar correlations were obtained for the other 14 myofibrils and are shown in the electronic supplementary material.

Rule 1 identified by Luther & Squire [33] and described above provides a clue to the basis of the distribution of filament rotations. The observation that filaments on an elementary triangle avoid all having the same rotation indicates that nearest-neighbour pairs of filaments prefer to adopt different, rather than the same, rotations. This indicates that the interaction energy between adjacent filaments of different rotations is lower than that between filaments of the same rotation. This corresponds precisely to the nearest-neighbour coupling for the classical TIA, as is described in the next subsection.

3.2. TIA correlations

We consider the classical TIA with only nearest-neighbour interactions, which is a two-state spin system on a triangular lattice, for which the interaction energy for opposite adjacent spins is lower than that for identical adjacent spins [1]. The energy between unlike adjacent spins is often denoted $-J$ and that between like spins $+J$, with $J > 0$. The energy difference is then $2J$, and to emphasize this, we denote it here by Δe, i.e. $\Delta e = 2J$. In our case then, Δe is the difference in the interaction energy between pairs of adjacent myosin filaments with like and unlike filament rotations.

The TIA is a well-studied, archetypal, geometrically frustrated system [1]. It is frustrated because it is impossible to minimize the energy of all three interactions on an elementary triangle, and if two spins have opposite orientations then the energy is independent of the orientation of the third spin (figure 5*a*). The nature of the distribution of the spins depends on the temperature of the system. We denote the actual, or environmental, temperature of the system by T_e. As a result of frustration, at $T_e = 0$ the system will adopt one of a large number of ground states. For $T_e > 0$, higher

energy states become more probable and the system becomes more random. For $T_e \to \infty$, the system becomes completely random. It is convenient, and common, to normalize the temperature against J and against Boltzmann's constant k, and to define a standard, or rescaled, temperature, which we denote T, by [51]

$$T = \frac{kT_e}{J} = \frac{2kT_e}{\Delta e}. \tag{3.2}$$

We use this rescaled temperature here.

Although Rule 1 suggests that the myosin superlattice disorder may be a manifestation of the TIA, verification requires a quantitative comparison of the spatial statistics of the observed myosin filament rotations with those of the TIA.

The second-order statistics of the TIA have been studied by a number of authors [51–53]. The spatial correlation function is complicated and not amenable to a simple analytical description. Although the correlation function $\rho(\mathbf{d})$ depends on the vector separation $\mathbf{d}$ between two lattice sites, i.e. equation (3.1), considerable simplification of its behaviour is achieved by partitioning the lattice into three sublattices, and expressing the correlation on each sublattice as a function of only the *distance* d between an origin and the sites on each sublattice. The sublattices are labelled 0, 1 and 2, and the corresponding correlation functions denoted by $\rho_0(d)$, $\rho_1(d)$ and $\rho_2(d)$, respectively. These three correlation functions, together, contain all the information on $\rho(\mathbf{d})$. The structure of the three sublattices is shown in figure 5*b*, and is described in detail in the appendix and in [51]. Each sublattice contains one-third of the lattice sites. An origin is chosen arbitrarily on the lattice, which defines a site on sublattice 0, and the remaining sites are assigned to one of the three sublattices as shown in figure 5*b*. We can then consider $\mathbf{a}$ in equation (3.1) to be the chosen origin and the vector $\mathbf{d}$ is from the origin to each other site (each belonging to its own sublattice) in the lattice. The averaging over $\mathbf{a}$ in equation (3.1) is then performed by shifting the origin to each point of the lattice. The result is three one-dimensional correlation functions $\rho_i(d)$ for $i = 0$, 1, 2, that together represent the two-dimensional correlation function $\rho(\mathbf{d})$. An advantage of this representation is that while $\rho(\mathbf{d})$ is a rapidly fluctuating function of $\mathbf{d}$, each $\rho_i(d)$ is a smoothly varying function of d.

Note that sublattice 0 is triangular with a lattice spacing of $\sqrt{3}$, where we take the spacing of the underlying triangular lattice to be unity, and connects second nearest neighbours of the underlying lattice (see figure 7 in the appendix), and therefore corresponds to the myosin filament superlattice as described above.

As noted above, the three correlation functions are complicated and not amenable to exact analytical calculation. However, for each sublattice, they decay approximately as $d^{-1/2}$ for $T = 0$, and for $T > 0$, there is an additional exponential decay, the decay rate increasing with increasing temperature [51,53]. The correlations are positive for sublattice 0 and, for small temperatures ($T < 1$), are negative for sublattices 1 and 2. The correlation functions are similar on sublattices 1 and 2. Approximate analytical expressions are available for the correlation function [52,53], but these are of limited accuracy, especially for $T > 0$. We have derived empirical approximations to the correlation function that are quite accurate [51] and we use these for the calculations presented here.

3.3. Fitting the micrograph rotation data to the TIA correlation function

In view of the sublattice structure of the correlations for the TIA, the correlations calculated from the micrograph and shown by the filled circles in figure 4 are plotted in three colours, one for each sublattice. The observed correlations are then seen to be smoothly varying functions of distance on each sublattice.

To assess the TIA as a model of the myosin filament rotation disorder, the TIA correlations are calculated and fitted to the micrograph correlation data. Since the myofibrils assemble at physiological temperatures, the resulting system will not be in the ground state. Therefore, the correlation function for the TIA is calculated for a range of rescaled temperatures T, with $\Delta T = 0.01$. For each temperature, the agreement between the correlation function from the micrograph data and that calculated for the TIA is measured by calculating the weighted root-mean-square difference (RMSD) (see the electronic supplementary material), with weights equal to the inverse of the squared standard error for each datum, between the observed and calculated correlations, for $1 \le d \le 6$. The RMSD is calculated over all three sublattices. We refer to the temperature that gives the best fit (smallest RMSD) as the effective temperature, denoted T_{eff}, of the system. The search over T is a means for searching over Δe via equation (3.2). This minimum value of the RMSD measures the quality of the TIA as a model of the observed spatial distribution of the myosin filament rotations.

For the micrograph shown in figure 2*a*, the above procedure results in an RMSD of 4%, indicating a good fit to the data, with an effective temperature $T_{\text{eff}} = 0.51$. The TIA correlation function at this temperature, for each sublattice, is shown by the curves in figure 4. The TIA correlations are shown as continuous curves in figure 4 for clarity, although they exist only at the discrete d values of the corresponding sublattice. The experimental and calculated values are compared by comparing the experimental points (filled circles) with the values on the curve of the same colour at the same value of d. Inspection of the figure shows good agreement between the measured and calculated correlations, within the error bars, and also indicated by the small RMSD. Even the rather subtly different behaviour of the correlations on sublattices 1 and 2 is seen in the data. For reference, if the distribution of the filament rotations were random, then the correlation function would be equal to zero for all $d > 0$, which clearly does not fit the data, and gives a significantly larger RMSD of 13.5%. The good agreement for the TIA strongly supports this model of filament rotations over a model of random rotations.

The same analysis was conducted for the 14 other myofibrils, and the measured and calculated correlation functions are shown in the electronic supplementary material. In all cases, significant correlations are seen out to a distance of 6 lattice spacings, indicating well-developed geometric frustration. The effective temperatures and corresponding RSMDs are listed in table 1. The small RMSDs indicate good agreement with the TIA model in all cases. Also listed in the table is the corresponding RMSD, for each micrograph, for a model of random filament rotations, and the ratio, denoted R, of this RMSD to that for the TIA model. Large values of R ($R > 1$) indicate the degree to which the TIA model is preferred over a random model. The RMSDs for the random model are all significantly larger than for the TIA model, with a ratio greater than three in most cases, indicating a strong preference

Table 1. Effective temperatures, T_{eff}, and RMSD, for the 15 myofibrils. N is the number of myosin filaments in the myofibril used for the correlation calculations.

			RMSD		
myofibril	N	T_{eff}	TIA	random	R
frog 1	552	0.51	0.040	0.135	3.38
frog 2	1660	0.55	0.016	0.118	7.38
frog 3	281	0.40	0.040	0.181	4.53
frog 4	578	0.49	0.043	0.144	3.35
frog 5	495	0.56	0.047	0.139	2.96
frog 6	476	0.42	0.034	0.172	5.06
frog 7	541	0.58	0.049	0.131	2.67
frog 8	497	0.50	0.037	0.143	3.86
frog 9	780	0.48	0.041	0.154	3.76
shark 1	310	0.76	0.053	0.089	1.19
shark 2	403	0.73	0.067	0.078	1.56
shark 3	1879	0.71	0.037	0.071	2.43
polypterus 1	637	0.52	0.023	0.123	5.35
polypterus 2	296	0.52	0.044	0.126	2.86
turtle	283	0.43	0.046	0.154	3.38

for the TIA model. The effective temperatures are similar at $T_{\text{eff}} \sim 0.5$ for most of the micrographs, indicating that the TIA represents a universal model of the superlattice disorder. An exception is the shark muscle myofibrils with $T_{\text{eff}} \sim 0.7$, although there is still a good fit to the TIA model, but with a different effective temperature. The value of R is smaller for the shark myofibrils, since the larger T_{eff} corresponds to a more random distribution of rotations.

4. Discussion and conclusion

Analysis of the second-order statistics of the myosin filament rotations in vertebrate striated muscle shows that the myosin superlattice is well described by the TIA. The degree of disorder is similar for all species except for the shark muscle, which shows more disorder.

The packing and the rotational relationships between the myosin filaments are fixed, and anchored in the M-band, during assembly of the sarcomere. The next sarcomere along the myofibril involves a different set of myosin filaments and a different M-band. The connection between two contiguous sarcomeres is through the Z-line (figure 1), which has a different symmetry from the myosin lattice. Therefore, the fibril assembly and packing in one sarcomere can be considered in isolation, independent of the other sarcomeres. The superlattice structure in one sarcomere as seen in the electron micrographs is therefore a two-dimensional (2D) phenomenon, determined by the energetics of the 2D Ising model as described here. Therefore, the effective temperatures determined here can be used to assess the energy difference that might contribute to the formation of the superlattice, as opposed to the simple lattice, in one sarcomere.

The energy difference, Δe, between like and unlike adjacent myosin filament rotations is estimated, using equation (3.2), as

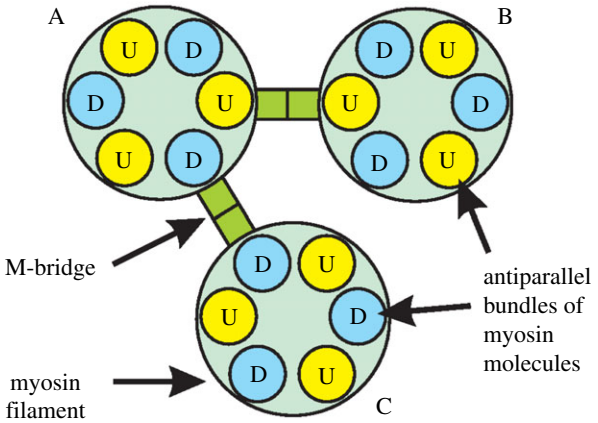

Figure 6. The interactions between three adjacent myosin filaments (A–C), where B and C have the same rotation, which is different from that of A. Each filament has threefold symmetry about the filament axis, which relates pairs of up (U) and down (D) bundles of parallel myosin molecules [33]. The preferred filament pair interactions A to B and A to C result in preferred M-bridge interactions between parallel (U to U or D to D) myosin molecules, compared to the U to D interaction, which is energetically less favourable.

$\Delta e = 2kT_e/T_{\text{eff}}$, where T_e is the temperature at the time of sarcomere assembly, which we take as a physiological temperature of 300 K. For the frog sartorius specimens, the average effective temperature is $T_{\text{eff}} = 0.50$, which gives $\Delta e = 10.0$ kJ mol^{-1}. This value is similar to the stabilization energies contributed by hydrogen bonds and other weak protein–protein interactions [54,55].

The relative rotation of adjacent filaments is expected to be driven primarily by the protein cross-links, or so-called M-bridges, in the M-band region (figure 1*b*). This interaction is believed to be mediated, primarily, at two positions on each filament, by two myomesin molecules at the M-bridges [34]. The energy difference Δe between the two different myosin filament pair rotations (like or unlike) in a single sarcomere is therefore expected to be dominated by these two myomesin cross-links.

The myosin filament backbone in the M-band region is made up of six bundles of myosin molecules, each bundle containing parallel molecules [33], with three bundles pointing up and three pointing down, as shown in figure 6. Pairs of up and down bundles are related by threefold symmetry (which is the source of the triangular cross-section seen in the bare-region micrographs). A consideration of the symmetry within the filament and the filament packing shows that with the preferred adjacent unlike rotations of the myosin filaments, the preferred interactions are between parallel, rather than antiparallel, myosin molecules (figure 6).

The preferred, i.e. lower energy, interaction between the parallel molecules is mediated by two M-bridges, suggesting an energy difference of about 5.0 kJ mol^{-1} per M-bridge or per myomesin molecule. Mutagenesis binding studies have shown that substitution of a single amino acid can disrupt protein–protein binding with an associated energy difference greater than 6 to 10 kJ mol^{-1} [56]. Therefore, sequence differences of one or two amino acids could be sufficient to differentially produce the superlattice or simple lattice structures.

We acknowledge that, since the detailed mechanism and energetics of the assembly of the myosin filament array are unknown, the above conclusions are somewhat speculative. However, they do provide some insight into the magnitude of molecular structural differences that might be involved. Furthermore, this approach illustrates how mapping a complex biological system to a statistical mechanical model can allow bulk observations (of

the pattern of filament rotations seen in electron micrographs in the current example) can potentially be used to infer characteristics (such as interaction energies) at the molecular level.

There is evidence that slow, fatigue-resistent muscle fibres are associated with the simple lattice and that fast, fatigable fibres are associated with the superlattice [37,43], suggesting that the lattice type may be involved in fine-tuning the mechanical behaviour of muscles. For example, if the superlattice structure allows more efficient sharing of actin binding sites by myosin heads, the greater number of actin–myosin interactions may contribute to the greater force production of fast, fatigable fibres [43]. Different M-line proteins of particular fibre types may interact sufficiently differently (energetically) with the myosin filaments to produce the different lattice types.

The other advantage of a rigorous physical description of disorder in such systems is that it can allow a rigorous derivation of other physical quantities. In the case at hand, since diffraction from a disordered system is a function of its second-order statistics, the long-range correlations from the TIA model open a route for accurate calculation of X-ray diffraction from muscle fibres, which would aid in interpretation of such data for structure determination.

In summary, we have shown that the myosin filament lattice in representative higher vertebrate striated muscles is a geometrically frustrated system—the TIA. This is a somewhat novel appearance of statistical physics in structural biology. The results indicate that the initial M-bridge crosslinking process may be driven by differences in the protein–protein interaction energies between differently oriented myosin and M-bridge molecules. The differences between the simple lattice and superlattice structures may be determined by sequence differences in myosin or the M-band proteins at the level of one or two amino acids. The resulting myosin head arrangement in the cross-bridge region is likely to be related to the nature of the myosin head–actin interactions during contraction, although the details of this require further study. The reason for the observed increased disorder in the shark muscle is also worthy of further study. The results should allow more accurate calculation of diffraction by model structures for comparison with muscle X-ray diffraction data.

Data accessibility. Data and information supporting this article are provided in the electronic supplementary material.

Authors' contributions. R.P.M. and J.M.S. conceived the research, all authors designed the study, conducted the analysis and analysed the results, and R.P.M., J.M.S., P.K.L., D.H.W. and C.H.Y. wrote the manuscript.

Competing interests. We declare we have no competing interests.

Funding. Funding was provided by the New Zealand Marsden Fund, the British Heart Foundation and the European MYORES network.

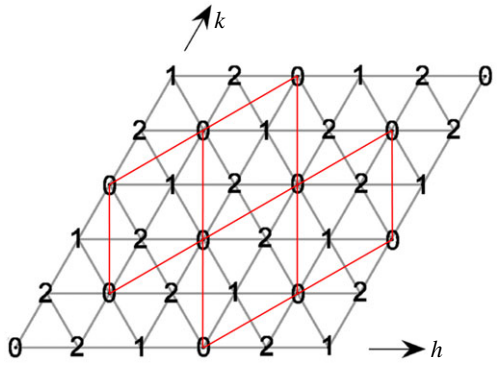

Figure 7. Sublattice structure for the sector $h \geq 0$ and $k \geq 0$. Sites labelled 0, 1 and 2 indicate the sites of sublattices 0, 1 and 2, respectively. The origin is at the lower left corner and is on sublattice 0. The rhombohedral superlattice joins the sites of sublattice 0, as shown in red.

Appendix A

The sublattice structure and the correlation function for the TIA are described in detail in [51]. Here, we provide a definition of the sublattices, and the reader is referred to [51] for more information.

The underlying triangular lattice is indexed by the integers (h, k) as shown in figure 7, which shows the 60° sector for $h \geq 0$ and $k \geq 0$. The sublattice (0, 1 or 2) to which each lattice point in this sector belongs is labelled in the figure. A precise definition of the lattice points belonging to each sublattice is as follows. In the 30° sector $h \geq 0$ and $0 \leq k \leq h$ in figure 7, the members of each sublattice are given by

$$\begin{aligned}
&\text{For sublattice 0:} \quad (h,k) = (3m, 3n) \qquad \text{for } m \geq 0 \text{ and } 0 \leq n \leq m \\
&\text{For sublattice 1:} \quad (h,k) = (3m+2, 3n) \text{ for } m \geq 0 \text{ and } 0 \leq n \leq m \\
&\text{For sublattice 2:} \quad (h,k) = (3m+1, 3n) \text{ for } m \geq 0 \text{ and } 0 \leq n \leq m,
\end{aligned} \tag{A 1}$$

for integers m and n. Denoting the sublattice membership of a lattice point (h, k) by the function $L(h, k)$, the sublattice membership of a point (h, k) in the 30° sector $0 \leq h \leq k$ and $k \geq 0$ in figure 7, is derived from those given in equation (A 1) by

$$L(h,k) = L(k,h) \quad \text{for } 0 \leq h \leq k \quad \text{and} \quad k \geq 0. \tag{A 2}$$

The sublattice assignment of the remainder of the lattice sites is generated by rotating the assignments in the 60° sector $h \geq 0$ and $k \geq 0$ (the sector shown in figure 7) by multiples of 60° about the origin $(h, k) = (0, 0)$. The result is then the sublattice structure shown in figure 5*b*. Sublattice 0 corresponds to the superlattice (shown in red in figure 7).

References

1. Wannier GH. 1950 Antiferromagnetism. The triangular Ising net. *Phys. Rev.* **79**, 357–364. (doi:10.1103/PhysRev.79.357)
2. Aeppli G, Chandra P. 1997 Seeking a simple complex system. *Science* **275**, 177–178. (doi:10.1126/science.275.5297.177)
3. Ramirez AP. 2003 Geometric frustration: magic moments. *Nature* **421**, 483. (doi:10.1038/421483a)
4. Mezard M. 2003 Passing messages between disciplines. *Science* **301**, 1685–1686. (doi:10.1126/science.1086309)
5. Moessner R, Ramirez AR. 2006 Geometrical frustration. *Phys. Today* **59**, 24–26. (doi:10.1063/1.2186278)
6. Harris M. 2008 Condensed-matter physics: the eternal triangle. *Nature* **456**, 886–887. (doi:10.1038/456886a)
7. Davidović D, Kumar S, Reich DH, Siegel J, Field SB, Tiberio RC, Hey R, Ploog K. 1997 Magnetic correlations, geometrical frustration, and tunable disorder in arrays of superconducting rings. *Phys. Rev. B* **55**, 6518–6540. (doi:10.1103/PhysRevB.55.6518)
8. Wang RF *et al.* 2006 Artificial 'spin ice' in a geometrically frustrated lattice of nanoscale ferromagnetic islands. *Nature* **439**, 303–306. (doi:10.1038/nature04447)
9. Nisoli C, Moessner R, Schiffer P. 2013 Colloquium: artificial spin ice: designing and imaging magnetic frustration. *Rev. Mod. Phys.* **85**, 1473–1490. (doi:10.1103/RevModPhys.85.1473)
10. Moessner R. 2001 Magnets with strong geometric frustration. *Can. J. Phys.* **79**, 1283–1294. (doi:10.1139/p01-123)

11. Welberry TR, Heerdegen AP, Goldstone DC, Taylor IA. 2011 Diffuse scattering resulting from macromolecular frustration. *Acta Crystallogr. B* **67**, 516–524. (doi:10.1107/S0108768111037542)
12. Tierno P. 2016 Geometric frustration of colloidal dimers on a honeycomb magnetic lattice. *Phys. Rev. Lett.* **116**, 038303. (doi:10.1103/PhysRevLett.116.038303)
13. Wang Y *et al.* 2018 Switchable geometric frustration in an artificial-spin-ice–superconductor heterosystem. *Nature Nanotech.* **13**, 560–565. (doi:10.1038/s41565-018-0162-7)
14. Wilfong B, Zhou X, Vivanco H, Campbell DJ, Wang K, Graf D, Paglione J, Rodriguez E. 2018 Frustrated magnetism in the tetragonal CoSe analog of superconducting FeSe. *Phys. Rev. B* **97**, 104408. (doi:10.1103/PhysRevB.97.104408)
15. Conde-Rubio A, Fraile Rodríguez A, Espinha A, Mihi A, Pérez-Murano F, Batlle X, Labarta A. 2019 Geometric frustration in ordered lattices of plasmonic nanoelements. *Sci. Rep.* **9**, 3529. (doi:10.1038/s41598-019-40117-4)
16. Moessner R, Sondhi SL. 2001 Ising models of quantum frustration. *Phys. Rev. B* **63**, 224401. (doi:10.1103/PhysRevB.63.224401)
17. Qi Y, Brintlinger T, Cumings J. 2008 Direct observation of the ice rule in an artificial kagome spin ice. *Phys. Rev. B* **77**, 094418. (doi:10.1103/PhysRevB.77.094418)
18. Mengotti E, Heyderman LJ, Fraile Rodríguez A, Bisig A, Le Guyader L, Nolting F, Braun HB. 2008 Building blocks of an artificial kagome spin ice: photoemission electron microscopy of arrays of ferromagnetic islands. *Phys. Rev. B* **78**, 144402. (doi:10.1103/PhysRevB.78.144402)
19. Ladak S, Read DE, Perkins GK, Cohen LF, Branford WR. 2010 Direct observation of magnetic monopole defects in an artificial spin-ice system. *Nat. Phys.* **6**, 359–363. (doi:10.1038/nphys1628)
20. Farhan A *et al.* 2013 Direct observation of thermal relaxation in artificial spin ice. *Phys. Rev. Lett.* **111**, 057204. (doi:10.1103/PhysRevLett.111.057204)
21. May A, Hunt M, Van Den Berg A, Hejazi A, Ladak S. 2019 Realisation of a frustrated 3D magnetic nanowire lattice. *Commun. Phys.* **2**, 13. (doi:10.1038/s42005-018-0104-6)
22. Han Y, Shokef Y, Alsayed AM, Yunker P, Lubensky TC, Yodh AG. 2008 Geometric frustration in buckled colloidal monolayers. *Nature* **456**, 898–903. (doi:10.1038/nature07595)
23. Irving M. 2017 Regulation of contraction by the thick filaments in skeletal muscle. *Biophys. J.* **39**, 539–557. (doi:10.1016/j.bpj.2017.09.037)
24. Eakins F, Knupp C, Squire JM. 2019 Monitoring the myosin crossbridge cycle in contracting muscle: steps towards 'muscle the movie'. *J. Muscle Res. Cell Motil.* **40**, 77–91. (doi:10.1007/s10974-019-09543-9)
25. Brunello E, Fusi L, Ghisleni A, Park-Holohan SJ, Ovejero JG, Narayanan T, Irving M. 2020 Myosin filament-based regulation of the dynamics of contraction in heart muscle. *Proc. Natl Acad. Sci. USA* **117**, 8177–8186. (doi:10.1073/pnas.1920632117)
26. Yamada Y, Namba K, Fujii T. 2020 Cardiac muscle thin filament structures reveal calcium regulatory mechanism. *Nat. Commun.* **11**, 153. (doi:10.1038/s41467-019-14008-1)
27. Wang Z, Grange M, Wanger T, Kho AL, Gautel M, Raunser S. 2021 The molecular basis for sarcomere organization in vertebrate skeletal muscle. *Cell* **184**, 2135–2150. (doi:10.1016/j.cell.2021.02.047)
28. Squire JM. 1981 *The structural basis of muscular contraction*. New York, NY: Plenum Press.
29. Squire JM. 1997 Architecture and function in the muscle sarcomere. *Curr. Opin. Struct. Biol.* **7**, 247–257. (doi:10.1016/S0959-440X(97)80033-4)
30. Huxley AF. 1974 Muscular contraction. *J. Physiol.* **243**, 1–43. (doi:10.1113/jphysiol.1974.sp010740)
31. Huxley HE, Brown W. 1967 The low-angle X-ray diagram of vertebrate striated muscle and its behaviour during contraction and rigor. *J. Mol. Biol.* **30**, 383–434. (doi:10.1016/S0022-2836(67)80046-9)
32. Eakins F, Pinali C, Gleeson A, Knupp C, Squire JM. 2016 X-ray diffraction evidence for low force actin-attached and rigor-like cross-bridges in the contractile cycle. *Biology* **5**, 27792170. (doi:10.3390/biology5040041)
33. Luther PK, Squire JM. 1980 Three-dimensional structure of the vertebrate muscle A-band: II. The myosin filament superlattice. *J. Mol. Biol.* **141**, 409–439. (doi:10.1016/0022-2836(80)90254-5)
34. Squire JM, Al-Khayat HA, Knupp C, Luther PK. 2005 Molecular architecture in muscle contractile assemblies. *Adv. Protein Chem.* **71**, 17–87.
35. Luther PK, Munro PMG, Squire JM. 1981 Three-dimensional structure of the vertebrate muscle A-band: III. M-region structure and myosin filament symmetry. *J. Mol. Biol.* **151**, 703–730. (doi:10.1016/0022-2836(81)90430-7)
36. Luther PK, Squire JM, Forey PL. 1996 Evolution of myosin filament arrangements in vertebrate skeletal muscle. *J. Morphol.* **229**, 325–335. (doi:10.1002/(SICI)1097-4687(199609)229:3<325::AID-JMOR7>3.0.CO;2-X)
37. Ma W, Lee KH, Yang S, Irving TC, Craig R. 2019 Lattice arrangements of myosin filaments correlates with fiber type in rat skeletal muscle. *J. Gen. Physiol.* **151**, 1404–1412. (doi:10.1085/jgp.201912460)
38. Yu LC, Steven AC, Naylor GRS, Gamble RC, Podolsky RJ. 1985 Distribution of mass in relaxed frog skeletal muscle and its redistribution upon activation. *Biophys. J.* **47**, 311–321. (doi:10.1016/S0006-3495(85)83921-7)
39. Malinchik S, Yu LC. 1995 Analysis of equatorial X-ray diffraction patterns from muscle fibers: factors that affect the intensities. *Biophys. J.* **68**, 2023–2031. (doi:10.1016/S0006-3495(95)80379-6)
40. Ma W, Gong H, Irving T. 2018 Myosin head configurations in resting and contracting murine skeletal muscle. *Int. J. Mol. Sci.* **19**, 2643. (doi:10.3390/ijms19092643)
41. Millane RP, Yoon CH, Blakeley ND, Goyal A. 2006 Analysis and modelling of substitution disorder in the myosin lattice of vertebrate muscle. *Proc. SPIE* **6316**, 63160D. (doi:10.1117/12.683426)
42. Yoon CH, Millane RP, Blakeley ND, Goyal A. 2007 Statistical modeling of the myosin lattice in vertebrate muscle. *Proc. SPIE* **6498**, 64981C. (doi:10.1117/12.722163)
43. Luther PK, Squire JM. 2014 The intriguing dual lattices of the myosin filaments in vertebrate striated muscles: evolution and advantage. *Biology* **3**, 846–865. (doi:10.3390/biology3040846)
44. Koubassova NA, Tsaturyan AK. 2011 Molecular mechanism of actin-myosin motor in muscle. *Biochem. (Moscow)* **76**, 1484–1506. (doi:10.1134/S0006297911130086)
45. Stroud WJ, Millane RP. 1996 Cylindrically averaged diffraction by distorted lattices. *Proc. R. Soc. Lond. A* **452**, 151–173. (doi:10.1098/rspa.1996.0009)
46. Welberry TR. 2004 *Diffuse X-ray scattering and models of disorder*. New York, NY: Oxford University Press.
47. Millane RP. 2010 X-ray fibre diffraction analysis. In *International Tables for Crystallography, vol. B. ch. 2.4* (ed. U Schmueli), pp. 568–583. Chester, UK: International Union of Crystallography.
48. Koubassova NA, Tsaturyan AK. 2002 Direct modeling of x-ray diffraction pattern from skeletal muscle in rigor. *Biophys. J.* **83**, 1082–1097. (doi:10.1016/S0006-3495(02)75232-6)
49. Yoon CH, Millane RP. 2014 Diffraction by a frustrated system: the triangular Ising antiferromagnet. *J. Opt. Soc. Am. A* **31**, 1416–1426. (doi:10.1364/JOSAA.31.001416)
50. Yoon CH *et al.* 2009 Determination of myosin filament orientations in electron micrographs of muscle cross sections. *IEEE Trans. Image Process.* **518**, 831–839. (doi:10.1109/TIP.2008.2011379)
51. Wojtas DH, Millane RP. 2009 Two-point correlation function for the triangular Ising antiferromagnet. *Phys. Rev. E* **79**, 041123. (doi:10.1103/PhysRevE.79.041123)
52. Stephenson J. 1964 Ising-model spin correlations on the triangular lattice. *J. Math. Phys.* **5**, 1009–1024. (doi:10.1063/1.1704202)
53. Stephenson J. 1970 Ising model with antiferromagnetic next-nearest-neighbor coupling: spin correlations and disorder points. *Phys. Rev. B* **1**, 4405–4409. (doi:10.1103/PhysRevB.1.4405)
54. Bosshard HR, Marti DN, Jelesarov I. 2004 Protein stabilization by salt bridges: concepts, experimental approaches and clarification of some misunderstandings. *J. Mol. Recognit.* **17**, 1–16. (doi:10.1002/jmr.657)
55. Wendler K, Thar J, Zahn S, Kirchner B. 2010 Estimating the hydrogen bond energy. *J. Phys. Chem. A* **114**, 9529–9536. (doi:10.1021/jp103470e)
56. DeLano WL, Ultsch MH, de Vos AM, Wells JA. 2000 Convergent solutions to binding at a protein–protein interface. *Science* **287**, 1279–1283. (doi:10.1126/science.287.5456.1279)